Article:
Zhao, J, Yao, G and Wen, D (2020) Salinity-dependent alterations of static and dynamic contact angles in oil/brine/calcite systems: A molecular dynamics simulation study. Fuel, 272. 117615. ISSN: 0016-2361

https://doi.org/10.1016/j.fuel.2020.117615

Salinity-dependent alterations of static and dynamic contact angles in oil/brine/calcite systems: A molecular dynamics simulation study

*Jin Zhao [1,3],Guice Yao [2], Dongsheng Wen [3,1, 2]**

AUTHOR ADDRESS

1. School of General Engineering, Beihang University, 100191, Beijing, P. R. China

2. School of Chemical and Process Engineering, University of Leeds, Leeds, LS2 9JT, U.K

3. School of Aeronautic Science and Engineering, Beihang University, 100191, Beijing, P. R. China

ABSTRACT

In this study, classic Molecular Dynamics (MD) simulations with established force fields were first performed to investigate the salinity effects on the static contact angle of a n-decane droplet immersing in the water atmosphere within a calcite nanochannel to advance our microscopic understanding on low salinity flooding. By applying an external body force, dynamic contact angle of n-decane in the water phase was also studied in the presence of various salt concentrations based on Non-Equilibrium MD (NEMD) simulation. The predicted n-decane static contact angles are around 59.68º ± 0.26º, which agree well with experimental results in previous studies. A reduction of the static contact angle of the nanodrop is observed with the increase of salinity, which implies an enhancement of surface hydrophilicity. Under flow conditions, the deformation of nanodrop, as evidenced by the centre of mass analysis, becomes faster by increasing the salt concentration. The recovery/mobility of the n-decane

nanodrop is, however, still significantly restricted by the adsorption interaction between the substrate and n-decane phase, which may lead to droplet snapping off and/or breaking up into small droplets.

KEYWORDS

Low salinity flooding; Molecular dynamics; Contact angle; NEMD; Enhanced oil recovery

1. INTRODUCTION

To meet increasing energy demand, enhanced oil recovery (EOR) has brought much attention and a variety of techniques have been investigated[1-3]. Low salinity flooding (LSF) method, also as known as smart water flooding, has been shown to be a promising and an environment-friendly method for EOR applications [4-7]. However the results are highly controversial. While a few field and laboratory experiments have shown some enhancement of oil recovery performance by LSF, others showed different results [8-14]. It has been shown that the EOR performance results are highly dependent on the brine components, salinity and many other factors such as rock permeability, pH environment and mineral types. The exact cause of different results from LSF, however, still remains unclear.

A few mechanisms have been proposed to explain the LSF effects, which include electrical double layer (EDL) effect, wettability alteration, and multi-component ionic exchange (MIE) [15-18]. However none of these mechanisms is conclusive due to the complex nature of a given system: the geometrical complexity of the pore structure, the physicochemical interactions between the substrates and the fluids, and the interfacial effects between saltwater and hydrocarbon mixtures. In a typical system, all these factors are intervened together and it is highly demanding to control accurately individual factors experimentally. To isolate and identify the key factors, modelling of multiscale processes taking place during LSF becomes

highly important [19, 20] Microscopically, oil displacement occurs at the oil/water/rock interface, where the presence of ions and their interactions with the substrate becomes very important.

Molecular dynamics (MD) simulation method has been proved to be a powerful tool to investigate the flow and displacement at the nanoscales[21-25]. MD tends to be more computationally expensive. But it is capable of fully resolving flow fields at the nanoscale , providing a natural way to explore molecular configurations on the surface, and to identify the most favourable adsorption mechanism. The investigations of static and dynamic contact angles among multiphases with MD simulation method have been mainly conducted previously [26-29]. For instance, Hong et al. [30] investigated the variation of static contact angle of a water droplet in equilibrium with a solid surface in the absence of a body force, and dynamic contact angles of water droplet moving on a solid surface using MD simulation. A constant acceleration was applied to each water molecule in order to consider the effect of moving water droplet. The results showed that the water droplet changed its shape with a larger advancing contact angle than the receding angle. Lee et al. [31] investigated statistic and dynamic behaviours of a water droplet on a substrate with various structured pillars at the nanoscale with MD simulation. The dynamic behaviour of the water droplet was induced by applying a constant force and revealed the effects of hydrophobicity of the solid substrate. Wu et al. [32] reported the contact angle and condensation behaviour of carbon dioxide (CO_2) droplets on a smooth solid surface through MD simulations for the first time. Numerical results showed that both the dropwise and film-wise condensation of CO_2 was achieved depending on the wettability of the Cu-like surface. Derksen et al. [33, 34] applied both lattice Boltzmann scheme and MD method to investigate a droplet sliding over a solid substrate under a shear flow configuration. The dimensionless sliding speed was found to be a unique function of the equilibrium contact angle at low Reynolds and capillary numbers.

It shall be noted that though some studies have been carried out to study the static and dynamic behaviour of a liquid droplet on a flat surface, little work has been conducted on the salinity effect, an area of fundamental importance to LSF. To address this issue, the classic equilibrium and non-equilibrium MD simulations are performed to investigate the salinity effect on both the static and dynamic contact angle of a n-decane droplet immersing in water atmosphere within a calcite nanochannel for LSF applications. This paper is organized in the following manner: Firstly, as a benchmark model, the static contact angle of n-decane immersed in the pure water is measured through MD simulations for verifying the applied force fields and simulation methods (Section 3.1). The salinity-dependent contact angle of the n-decane nanodroplet is investigated by varying the salt concentration in the aqueous phase to identify its effect on the substrate wettability (Section 3.2). The dynamic contact angle of n-decane nanodroplet is further studied in two different sized nanochannels through NEMD simulations (Section 3.3). Finally the effect of water salinity on the dynamic contact angle is revealed and compared (Section 3.4) in terms of droplet deformation, average centre-of-mass moving speed and their sensitivity to the salinity.

2. MOLECULAR MODEL AND SIMULATION DETAILS

2.1 Model Construction

The initial configurations of the simulation models, consisting of two-phase fluids confined between two parallel solid plates, as illustrated in Figure 1, were generated by the Packmol package [35] and visualized by VESTA package [36, 37]. Two walls of each nanochannel were both composed by flat calcite {1 0 4} slabs with each length of 21.0 nm. The geometry size of the simulation box in y-axis direction was 30 Å. Seven layers of calcite atoms composed of each calcite slab with a thickness of 20 Å. In addition, two systems were established with channel widths of 8.5 nm to 12.0 nm, respectively, to consider the width effect,

as shown in **Figure 1(a, b)**, named by Model C1 and C2 systems, respectively. The system was initialized by immersing a rectangular block of n-decane ($C_{10}H_{22}$) molecules in water (H_2O) molecules inside the pore region, as a benchmark model. Model C1 composed of 577 n-decane molecules and 12569 water molecules; Model C2 composed of 330 n-decane molecules and 20948 water molecules. As a result, the channels for both models were filled with both n-decane and water molecules with the bulk density $\rho_{\text{n-decane}}$ and ρ_{water} of 730 and 997 kg/m^3, respectively. Aiming to identify the salinity effect on the static/dynamics contact angle, both sodium and chloride (NaCl) ions were further inserted randomly into the water phase to represent the aqueous electrolyte solution with the concentration in a range of 0 to 58,500 ppm. The maximum salinity of 58,500 ppm (~ 1 M NaCl solution) is considered from a similar level of the typical seawater salinity (i.e.,around 50 kppm) and the nature of LSF .

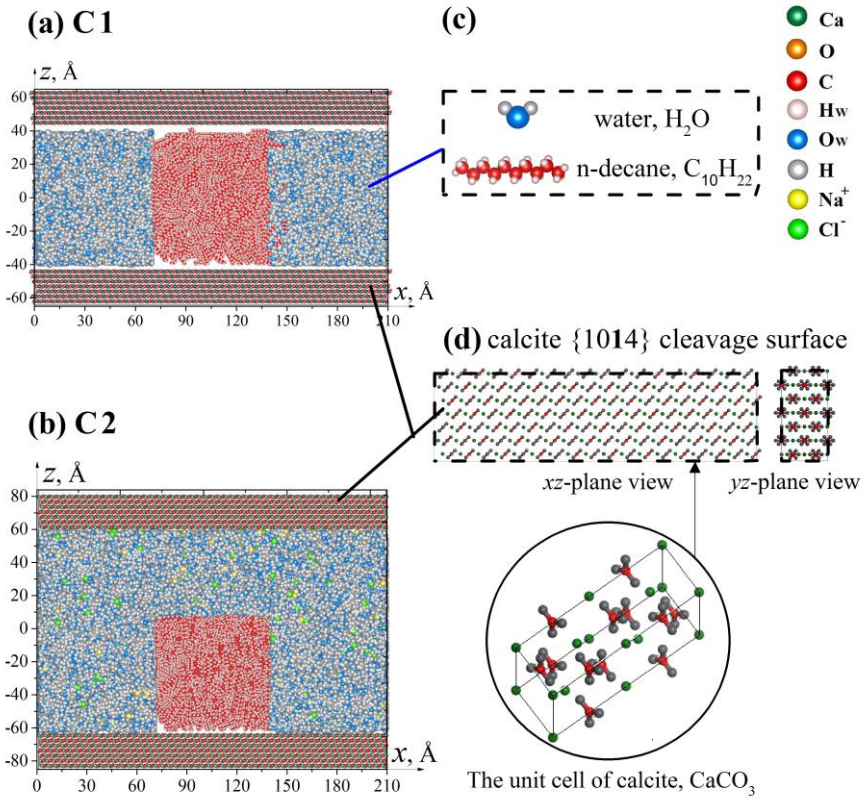

Figure 1 Snapshots of intial n-decane box immersed in aqueous phase confined in a calcite nanopore with two different pore widths

2.2 Simulation details

The model developed by Raiteri et al. [38] was employed to describe calcite surfaces. In the presented work, the Simple Point Charge/Extended (SPC/E) force field [39] was applied for water phase and the OPLS-AA (Optimised Potentials for Liquid Simulations – All Atoms) force field [40] was utilized to describe n-decane interactions. The sodium and chloride ions were modelled as charged Lennard-Jones particles using the parametrizations of the OPLS-AA force field. These force fields have tested extensively and applied successfully in a few previous simulations [41]. Details about the above force field parameters are listed in Table S1 and S2 (in the Supplementary Material).

The functional form of total energy U_{total} is written as Equation (1), including both the intra- and intermolecular interactions:

$$U_{\text{total}} = U_{\text{intramolecular}} + U_{\text{vdW}} + U_{\text{coulombic}} + U_{\text{external}} \quad (1)$$

$U_{\text{intramolecular}}$ describes all stretching and bending bonded interactions; the terms of U_{vdW} and $U_{\text{coulombic}}$ describe the van der Waals and electrostatic non-bonded interactions, where Lennard-Jones (LJ) 12-6 potential is used to represent the van der Waals interactions between different atomic species with geometric combining rules, and a cut-off distance of 1.2 nm is applied for the short-range van der Waals interactions with a precision of 1×10^{-6}; Smoothed Particle Mesh Ewald method is applied for the long-range interactions. U_{external} represents an external field potential, which is applied to predict the dynamic behaviour of the nanodrop.

All simulations were performed by the DL_POLY package [42] and periodic boundary conditions were imposed in all directions at ambient conditions of temperature and pressure. It is understood that the fluid confined in nanopores is generally at conditions with relative high temperature and pressure in geological environment. However, it is still necessary to run the simulations at ambient rather than reservoir temperatures, as the available calcite force field

has been parameterized to model systems under ambient conditions. Considerable validation would be required to ensure the force field holds for higher temperatures and pressures, work presently ongoing as future studies.

In this work, all simulations were run under the ambient conditions, a pressure of 1 bar, and a temperature of 300 K using a velocity scaling method. The canonical ensemble (NVT) was applied in the simulation models with the velocity rescaling Berendsen thermostat and Berendsen barostat. The equations of motion were solved by the leap-frog algorithm with a SHAKE subroutine with a time step of 0.5 fs. The position and velocity of each atom were updated and recorded each timestep. Finally, production runs of 2 ns were performed in the NVT ensemble and all equilibrium analyses were carried out over the last 2 ns of the simulations.

To study the n-decane nanodroplet motion affected by flow velocity, a body force F_x of 1.661×10^{-14} N scaled by each atom mass was applied along the positive x direction to all liquid atoms after the equilibrium of oil/brine/calcite system. This external body force value is considered as an equivalent value of 0.001 kcal/(mol·Å), which provides a large pressure gradient to the fluid flow confined in the calcite nanopore. This large value is necessary because the fluid flow through pores is slow, and it would take an extremely long simulation to achieve a stable flooding state. This ensures that each atom experiences the same acceleration, and consequently, both the n-decane droplet and aqueous phase move together in the positive x direction under a constant acceleration. The radial distribution function (RDF), density distribution, static contact angle and dynamics contact angle were calculated by analysing the trajectories of all molecules to reveal the fundamental salinity effects on static/dynamics contact angle alterations.

3. RESULTS AND DISCUSSION

3.1 Static Contact Angle

The validation of our simulation is demonstrated by a benchmark equilibrium MD simulation of the n-decane phase immersed in pure water confined in a nano calcite slit. In initial simulation configurations of C1 and C2 systems, rectangular n-decane boxes were created, surrounding by water molecules, all confined in calcite nanopores with different pore width (details of the two initial configurations have been outlined in Section 2.1).

It is notable that, at the molecular scale, the determination of contact angles for nanodroplets is challenging due to the continuous fluctuations of droplet shape. Using one or a few two-dimensional projections of a few snapshots can thus potentially lead to large errors on the measured contact angle, i.e., could be as large as 10° [43]. In order to accurately estimate the average contact angle during an MD simulation, the static contact angle is calculated based on five series of density profiles in the x-z plane with each slice thickness of 5.0 Å after the achievement of the equilibrium. The n-decane density contour plot is obtained by averaging each slice density over an additional 2.0 ns trajectories after 5ns' MD simulations. After obtaining the density contour plot of the static droplet on the flat calcite surface, the n-decane droplet periphery is then identified from the density contour using a least-squares circle fitting method. The points of the periphery below a height of 5.0 Å and above a height of 50.0 Å are not considered for the fit, to avoid the density fluctuations at the fluid-fluid and fluid-solid interface, which are illustrated in Figure 5 as highlighted. The static contact angle of n-decane droplet is determined as the angle between the tangential line of the fitted droplet surface and the horizontal line representing the liquid/solid interface.

The final snapshots of the equilibrated C1/C2 systems after 5 ns are illustrated in **Figure 2(a)**. For both systems, instead of water/n-decane mixing, there is a clear interface appealing

between these two phases. All n-decane molecules aggregate together to form a droplet-like shape with parts of the droplet surface directly adsorbing onto the calcite surface. The corresponding water and n-decane atomistic number density profiles along the axis normal to the calcite walls (z direction) were evaluated from the atomic trajectories of a 2.0 ns MD simulation after the equilibrium, as presented in **Figure 2(b)**. For C1 system, the n-decane nanodropet is attached onto both upper and lower calcite slabs after the equilibrium. Two major peaks of the related z-density distribution for both water and n-decane phases are observed in the near-wall region. The larger density of water and n-decane in the near-wall region shows their adsorption effects closing to the calcite surface. This effect diminishes as the distance increasing from the solid surface, indication of a bulk-like region. In terms of C2 system, the number density profiles of water and n-decane are asymmetric with respect to the central plane (z = 0) with intense oscillations near the walls, also indicating the layering structure of water and n-decane molecules in the near-wall region due to the prominent attractive force of the solid surface.

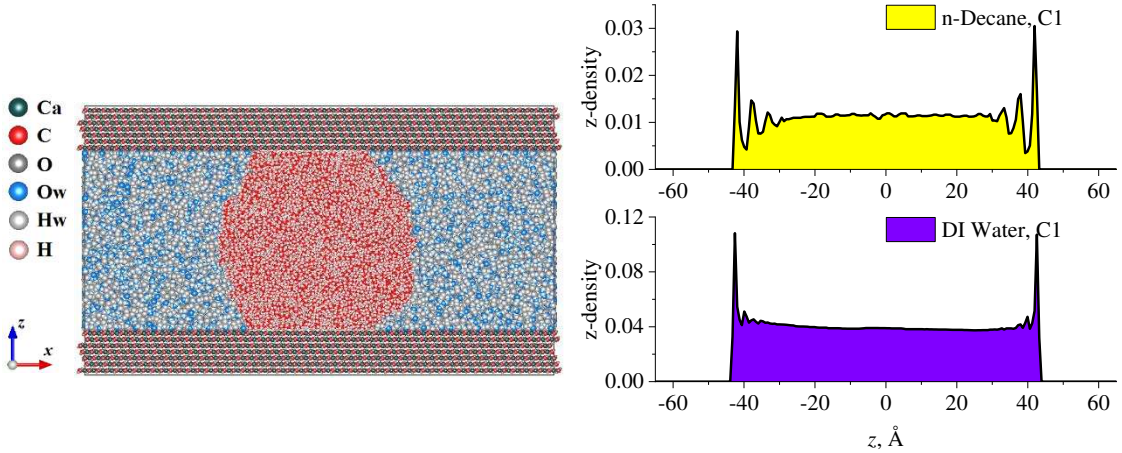

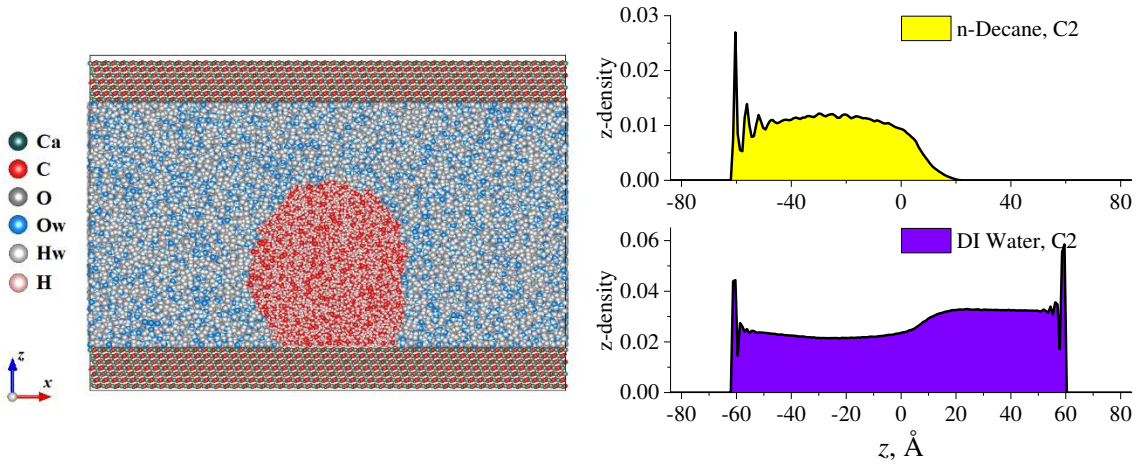

(a) Snapshots of C1/C2 systems in *x*-*z* plane after equilibrium

(b) Corresponding number density profiles of n-decane and DI water phases along the axis normal to the calcite walls (*z* direction) for C1/C2 systems

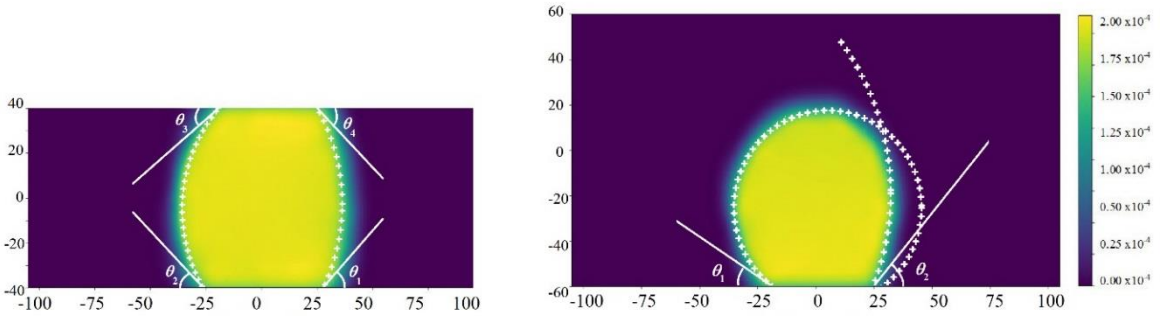

(c) Time-averaged planar density contour of n-decane droplet in the calcite nanopore with an illustration of static contact angle prediction: the white dashed curve is a fit to the droplet surface, the white line denotes the tangential line of the droplet surface

Figure 2 Equlibirum analysis for C1/C2 systems: (a) Snapshots along the axis normal to calcite surfaces after the equilbrium; (b) corresponding number density distribution; and (c) time-averaged planar density contours of n-decane droplet in a calcite nanopore with an illustration of static contact angle prediction

Visualized from the curvature shape of the water/n-decane interfaces as shown in **Figure 2(a)**, the calcite slabs exhibit more hydrophilicity for both C1/C2 systems. Furthermore, to specify the wettability of calcite substrate, the static contact angle of n-decane nano-droplet immersed in pure water is calculated based on the time-averaged n-decane planar density contours after the equilibrium of 2.0 ns, as presented in **Figure 2(c)**, where white dashed curve denotes a least-square circle fit to the water/oil interface to characterize the surface of n-decane

droplet, and the white line corresponds to the contact angle. The static contact angles of n-decane droplets immersed in pure water are determined by averaging among four contact angles for C1 system (similarly, averaging between two contact angles for C2 system), as illustrated in **Figure 2(c)**. The static contact angle is averaged twice to eliminate the nature fluctuation of MD simulations. It is indicated that the predicted n-decane contact angles for both C1 and C2 systems are around 59.68º ± 0.26º. The static contact angle of decane droplet on calcite plate immersed in water from the work of Metin et al [45] was given as a value of 58º; the water-oil contact angle on calcite plates was from Gupta et al. [44] reported as a value of 64º; etc. The reasons for varied values reported n-decane contact angle on the calcite substrate are multi-factoral, including different purity quotient of n-decane samples, different exposure cleavage surface of calcite substrate besides the {1014} surface and different roughness of calcite surface at the nanoscale applied. Taking above these factors into consideration, the predicted n-decane contact angles in this work (59.68º ± 0.26º) can be seen as a good agreement with experimental results reported previously [44-46]. In addition, according to the results obtained from the present computations, the values of n-decane static contact angle are not influenced significantly by the height of the calcite nanopore.

The intermolecular radial distribution functions (RDF) analysis of all species is used to identify the structural arrangement of molecules, defined as the probability of finding a pair of atoms within a certain distance. Representative results of RDFs for C2 system are shown in **Figure 3**. The observation RDF profiles for both n-decane bulk phase and water bulk phase, as shown in Figure 3(b) are consistent with previous experimental and simulation results with no shifts for the two main peaks [47, 48]. At longer distances, g(r) between two water molecules (or between two n-decane molecules) approaches a value of 1 as expected, indicating there is no long-range order for water phase (or oil phase). No significant peaks can be observed for the water/oil RDF profile in Figure 3(b), but only a continuously increasing trend, which is

consistent with the immiscibility of water and n-decane phases. The RDF profile of decane/calcite interactions and water/calcite interactions can be found in Figure 3(a). The sharp peak in calcite/water RDF profile at 2.6 Å suggests that water is adsorbed on both neutral and charged surfaces, consistent with the MD results of Cooke et al. [49]. The first peak for calcite/decane RDF profiles occurs at around 3.5 Å, which is larger than the position of first water/calcite RDF peak. It indicates the hydrophilicity of calcite substrate.

Such consistence also demonstrates that the validation of the present MD simulation methodology for the invesitgation of this complex multiphase system.

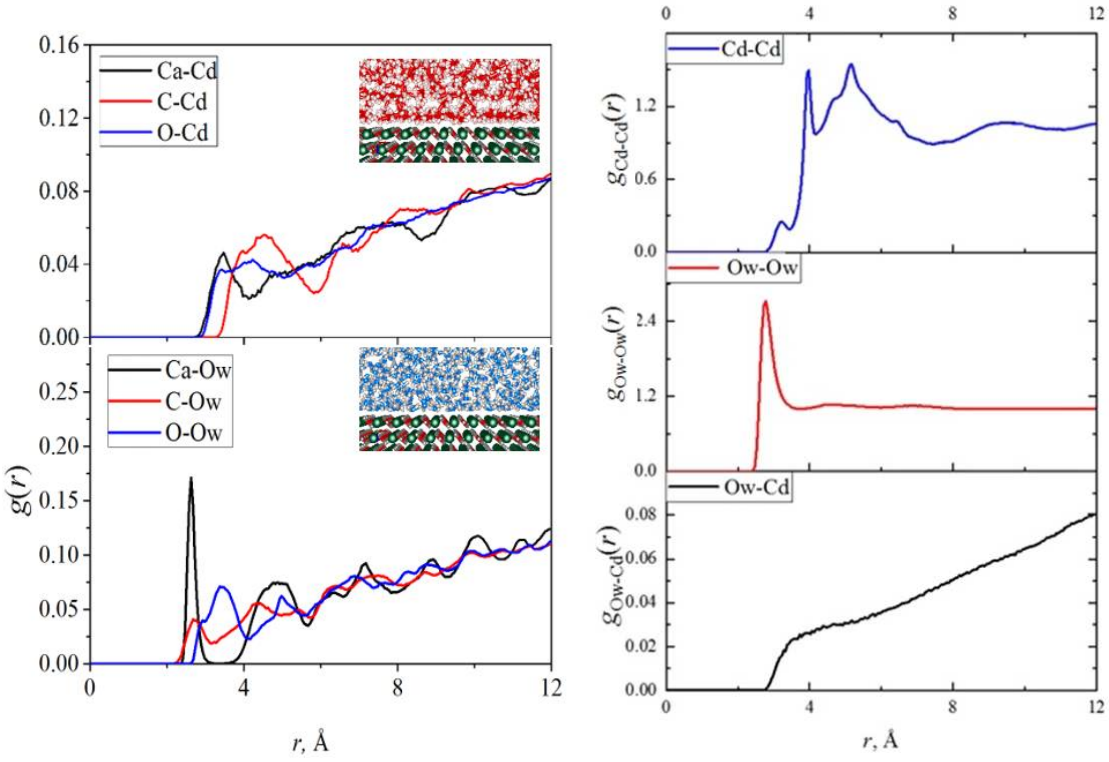

(a) (b)

Figure 3 Illustrations of RDFs; Left: Calcite-Oil (top) and Calcite-Water (bottom) RDFs for C2 systems; Right: Oil-Oil (top), Water-Water (middle) and Water-Oil (bottom) RDFs for C2 systems.

3.2 Effect of Salinity on Static Contact Angle

Through varying the salinity of water phase in a range of 0 to 58,500 ppm, the effect of sodium chloride concentration on the static contact angle of n-decane droplets immersed in aqueous electrolyte solutions is investigated in this session. To reveal the mechanism of the salinity-dependent contact angle, the density distribution of both water and n-decane molecules along the length (x) and height (z) direction are analysed in **Figure 4**. For C1 system, a slight shift of the water/n-decane interface can be observed in **Figure 4(1)** due to the presence of NaCl electrolyte in aqueous phase. Similarly, as illustrated in **Figure 4(2)**, the height of oil droplet decreased slightly with increasing salt concentration in the aqueous phase, which suggests that a higher salinity leads to a smaller contact angles and the oil droplets becomes wider.

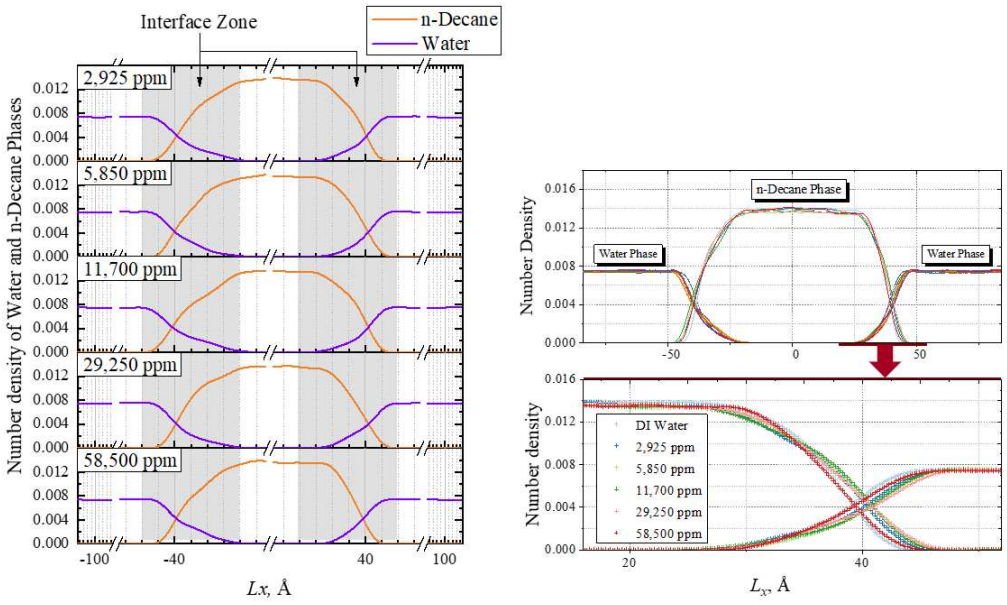

(1) Model C1

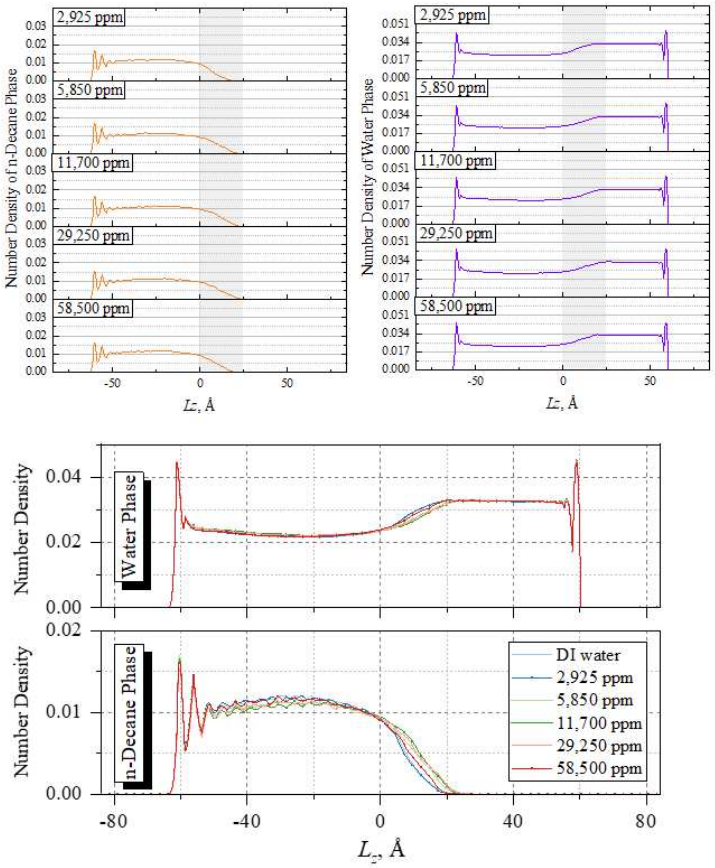

(2) Model C2

Figure 4 Salinity-dependent number density profiles of water and n-decane phases for C1/C2 systems

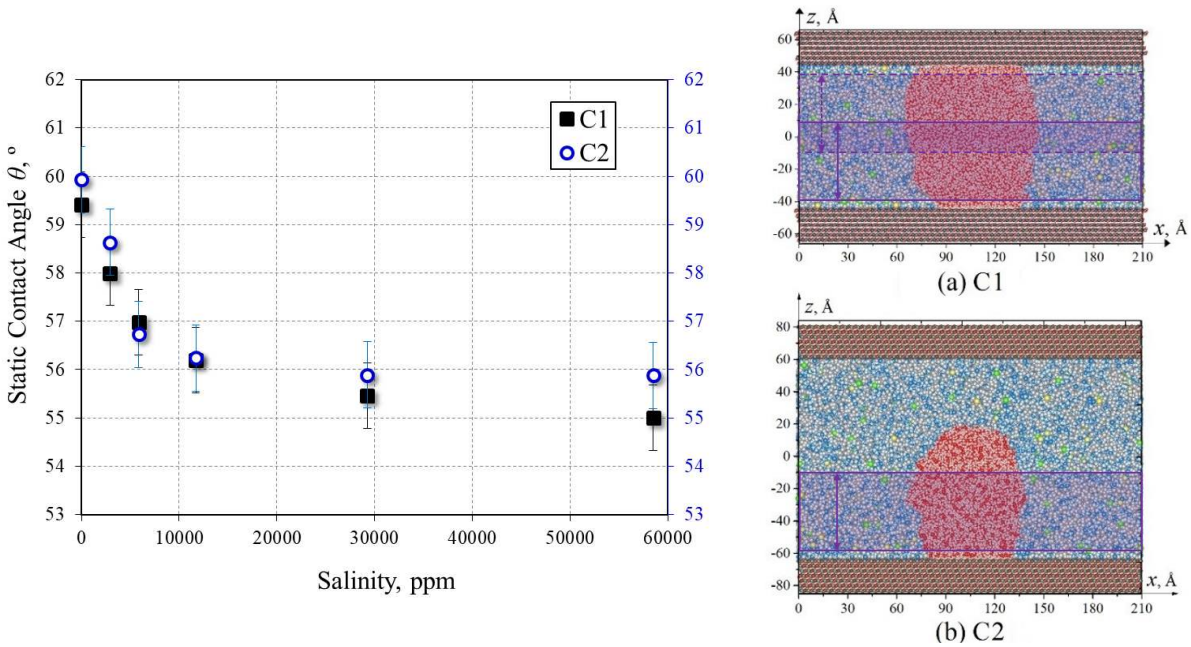

Figure 5 Variation of static contact angle with water salinity for C1 and C2 systems

The equilibrium contact angle of n-decane droplets in the calcite nanochannel as a function of water salinity is shown in **Figure 5**, with the illustrating snapshots of equilibrated C1 and C2 system with water salinity of 58,500 ppm. The result shows that the effect of salinity on the static contact angle of n-decane droplet is mild. The presence of NaCl electrolyte in aqueous phase reduces the static contact angle of n-decane droplet on calcite slabs from 59.41º to 55.02º for Model C1, and from 59.94 to 55.89º for Model C2, respectively, which demonstrates a slight enhancement effect of water salinity on the surface hydrophilicity.

It is worth to note that the reduction of static contact angle shows almost linearly when the water salinity increases from 0 to around 10,000 ppm, but this decrease trend weakens when the water salinity increases further. The width of calcite nanopore does not influence n-decane static contact angle significantly for both C1 and C2 models in this study.

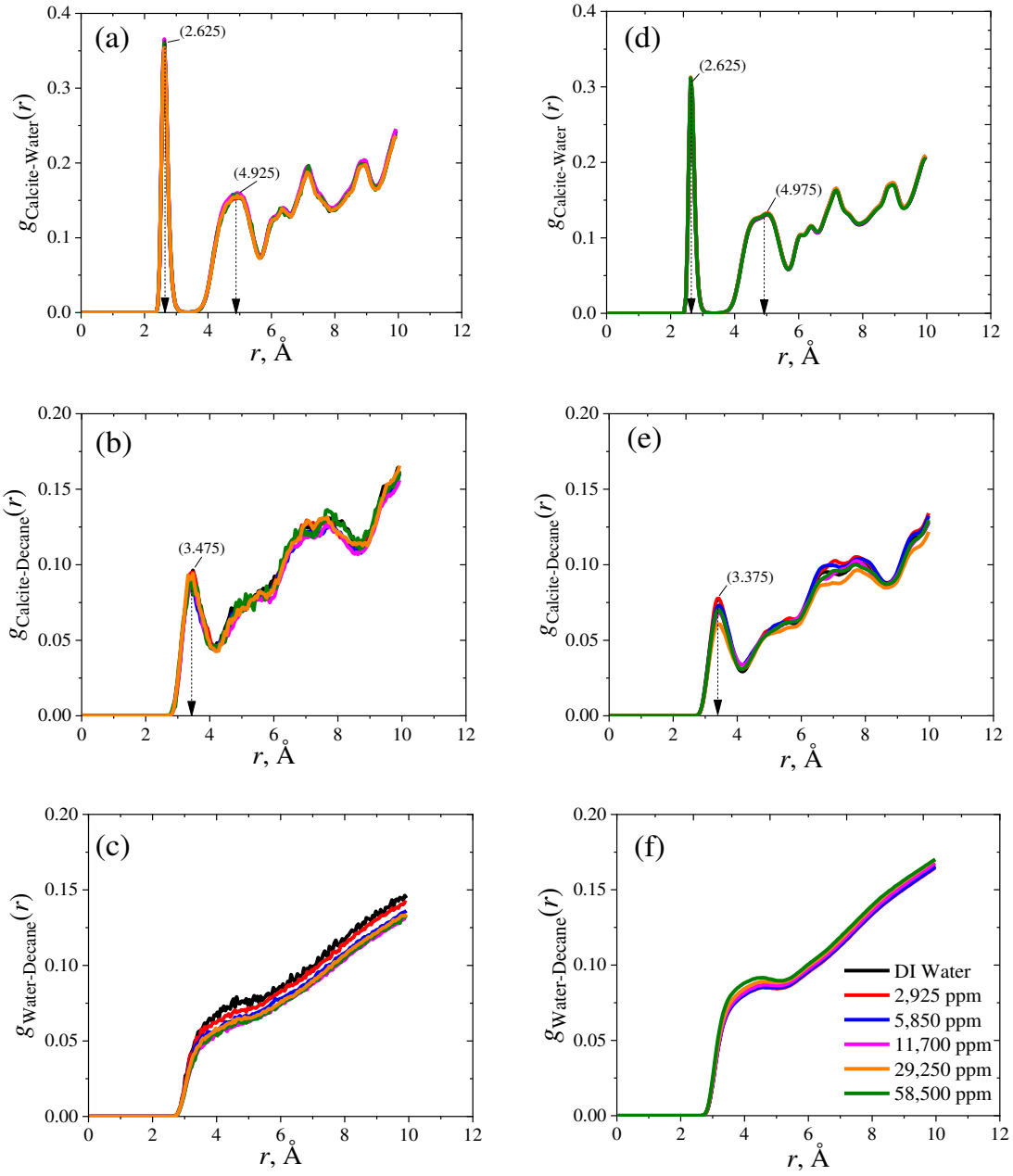

(1) C1 (2) C2

Figure 6 Salinity-dependent RDF plots of water/n-decane/calcite interactions for C1 and C2 systems

The RDFs for both C1 and C2 systems obtained from the simulation are compared in **Figure 6**. It can be seen from **Figure 6(a & d)** that, for both C1 and C2 systems, the presence of ions has little effect on the interactions between water and calcite. On the contrary, the

interaction between water and n-decane is affected by the ion presence as presented in **Figure 6(c & f)**. This phenomenon implies that the hydrophilicity variation of the slab surface is induced more likely from the salinity effects on the interfacial interactions between the water and n-decane interface. In addition, the interficial interaction variation induced by the presence of salt is limited, even at the concentration of 58,500 ppm, which cannot dramatically alter the wettability of the calcite slab significantly and detach the n-decane droplet from solid surface.

3.3 Dynamics Contact Angle

To observe the dynamic contact angle, a body force F of 1.661 $\times 10^{-14}$ N along the positive length (x) direction is applied to both equilibrated C1/C2 systems with no salt presence in the water phase. To characterize the dynamic advancing and receding contact angles of n-decane droplets in the calcite nanopore, the temporary dynamic advancing contact angle is extracted from the trajectories as the temporary angle obtained by extrapolating the fit of the advancing contact line to the line formed by the flat surface, and the temporary dynamic receding contact angle is obtained similarly [50-52].

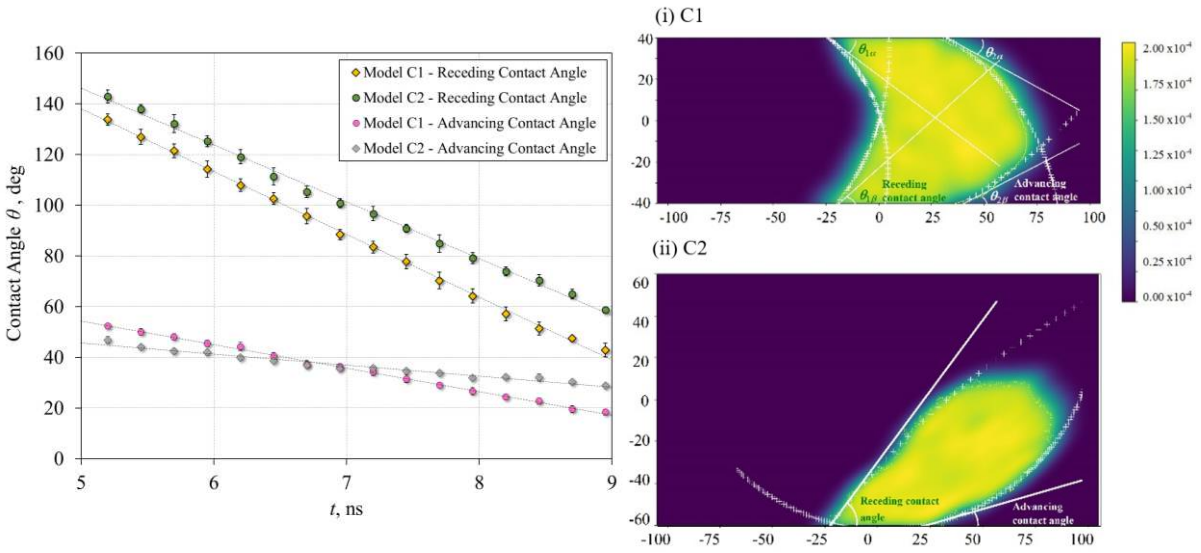

(a) (b)

Figure 7 Evolutions of dynamic contact angle (a) with illustrations of dynamic contact angle prediction (b)

By averaging the temporary dynamic contact angles in every 250 ps, the representative advancing and receding contact angle variations as a function of time are illustrated in **Figure 7**: the advancing and receding contact angle developments of n-decane droplets in the calcite nanochannels are compared in **Figure 7(a)**, associating with the illustration of the measurement method, as presented in **Figure 7(b)**. It can be seen that the advancing contact angle continuously reduces as a function of time due to the invading fluid, similar to that of the receding contact angle . In addition, it can be found from **Figure 7(a)** that the development rate of n-decane nanodroplet dynamics contact angle is influenced by the width of the calcite slits. The evolution of n-decane dynamics contact angle in C1 system is faster than that in C2 system. This is due to an additional attaching interaction between n-decane and the upper calcite slab in C1 system, comparing with that in C2 system.

3.4 Salinity-dependent Dynamics Contact Angle

To identify water salinity effect on the dynamic contact angle of n-decane nanodroplet immersed in the water phase within a calcite nanoslit, six salinities are considered in a range from 0 ppm (DI water) to 58,500 ppm. **Figure 8** demonstrates the temporary advancing contact angle evolutions as a function of time, considering different effects of salt concentrations in the water phase. The corresponding configuration snapshot in the *x*-*z* plane is also illustrated in **Figure 8** for Model C1 and C2. The linear-like trend between advancing contact angle and time can be observed for each cases with various channel widths and water salinities. Moreover, the decreasing of dynamic contact angles is faster with the increase of water salinity for both models. For Model C1, the invading fluid pulls the droplet forward, reshaping it from droplet-

like to concave-like shape. But during this period of time, the invading fluid does not flow through the oil phase yet. The slopes of the linear-like curves are shown more or less similar, whereas the intercepts of them shows various due to the effect of different salinities. For Model C2, the adsorption force for the oil droplet only comes from the bottom wall. During the flooding process, the invading fluid can flow through the space above the droplet. The salinity difference of the invading fluid can attribute to the dynamic contact angle variations with time. The higher salinity of water would cause smaller advancing contact angle with the evolution of time. Overall, larger slopes can be found when the salinity of water is higher for Model C2. It is notable that, for Model C2, as an evolution of time to 9.0 ns (t_2), the advancing side of the droplet exhibit a complex shape with no longer a circle-like curvatures. A snapped-off of the droplet might be occurred when the flooding process is further developed.

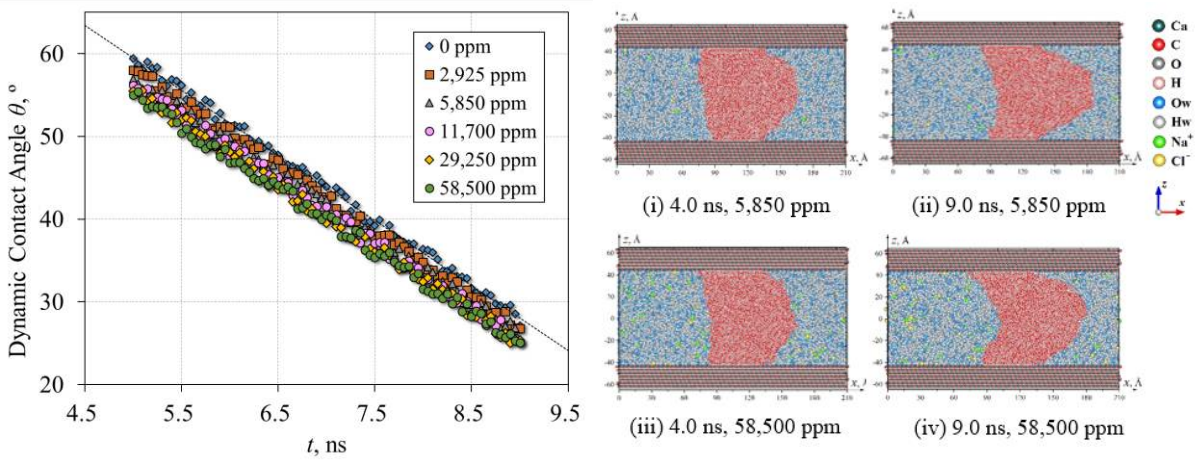

(a) Model C1

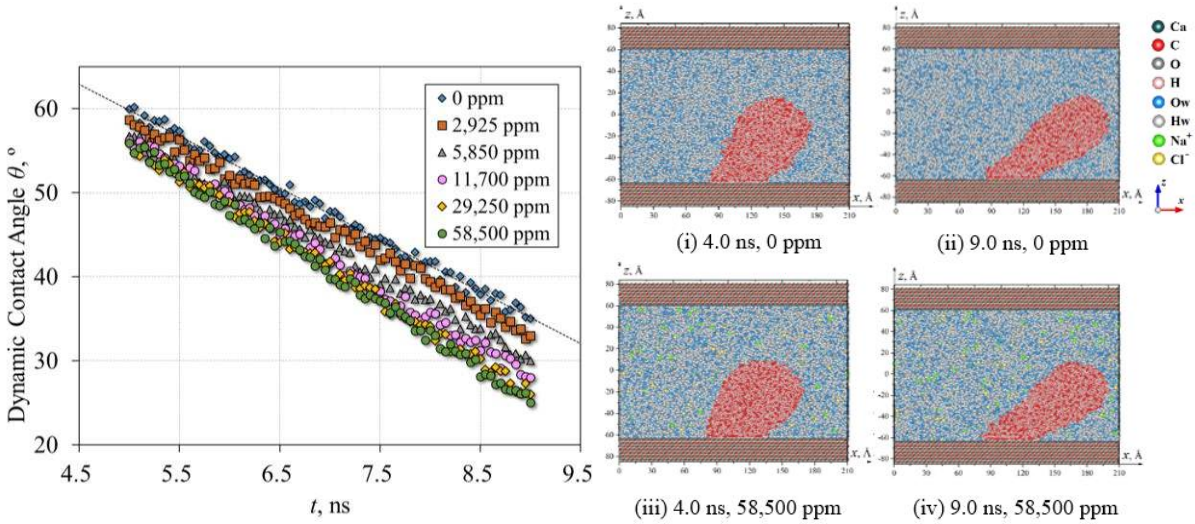

(b) Model C2

Figure 8 The advancing and receding contact angle evolution as a function of time

Figure 9(a) summerizes the results of the average velocity profiles for both C1 and C2 nanochannels with various salinity environments, estimating from traking the certer of mass (COM) evolutions of the n-decane nanodroplet trajectories, as presented in **Figure 9(b)**. A proportional relationship of the invading fluid salinity and n-decane nanodroplet average velocity is observed for both C1 and C2 systems. This result reveals that under the same flooding acceleration, the higher salinity of the invading fluid can lead to the faster COM evolutions for the motion of n-decane nanodroplet. Comparing the results between C1 and C2 simulation systems, the average advancing velocities of n-decane nanodroplet in C2 channel is greater than that in C1 channel. This result is induced by the indirect attachment between the n-decane nanodroplet and the upper calcite mineral surface in C2 systems with larger channel width, where less adsorption interactions are implied to the nanodroplet to prohibit its forward motion.

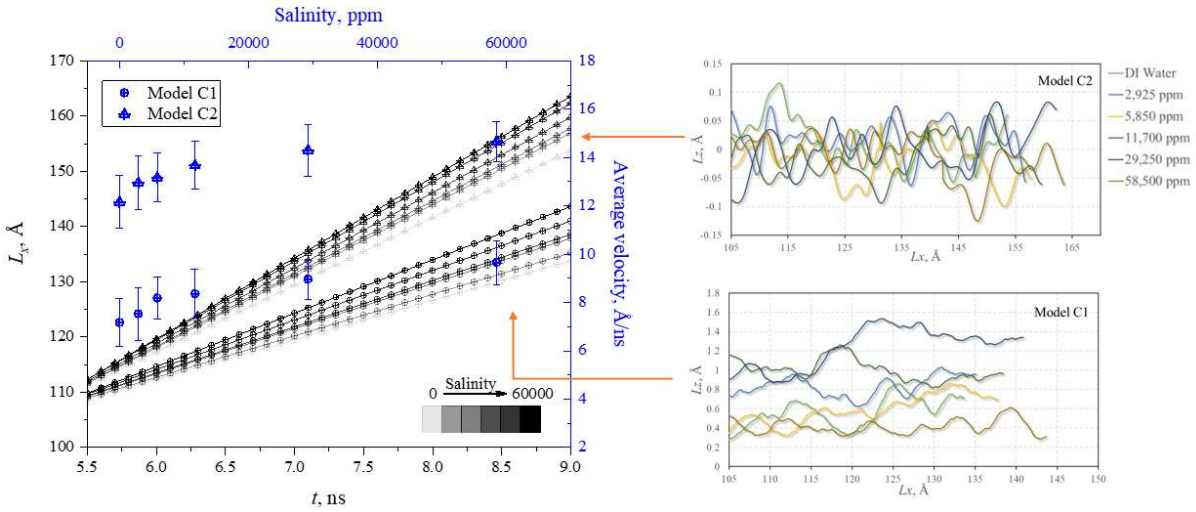

(a) (b)

Figure 9 The salinity-dependent velocity profiles with COM evolution trajectories at the molecular level

4. CONCLUSIONS

The salinity-dependent alterations of both static and dynamic contact angles of n-decane nanodrop embedded in different brine phases were investigated by both EMD and NEMD simulation methods. Two different widths of nanochannel were considered to identify different attaching situations of decane droplet. The simulation results can be concluded as followed:

(1) The static contact angle of n-decane nanodrop decreases with the increase of water salinity. It demonstrates the salinity effect on the enhancement of the surface hydrophilicity, which is mainly induced by influencing the water/n-decane interface as shown by RDF analysis. However, the effect of salinty on the surface wettability become weakened beyond a salinity of 10,000 ppm.

(2) The nanochannel width has few effect on the value of the static contact angles under different water salinity environments. For the dynamic contact angle evolutions, however, the nanodrop in the wider channel shows better movement performance, due to the less adsorption interactions between the solid slab and n-decane droplet.

(3) The COM evolution of n-decane nanodroplet along the invading fluid direction is salinity dependent. With the increase of water salinity, the defomation of the nanodrop becomes faster. However, due to the limited enhancement of the solid substrate wettability, the movement of n-decane is still significantly restricted by the adsoption interaction between calcite slab and n-decane phase. This constraint may lead to the droplet snapping off and /or breaking up into two small droplets with further increase of the flooding velocity.

ACKNOWLEDGEMENT

Financial support from European Research Council Consolidator Grant (Grant Number: 648375) is fully acknowledged.

AUTHOR INFORMATION

Corresponding Author

Email: d.wen@buaa.edu.cn and d.wen@leeds.ac.uk

Notes

The authors declare no competing financial interest.

REFERENCES

[1] Muggeridge A, Cockin A, Webb K, et al. Recovery rates, enhanced oil recovery and technological limits[J]. Philosophical Transactions of the Royal Society A: Mathematical, Physical and Engineering Sciences, 2014, 372(2006): 20120320.

[2] Alvarado V, Manrique E. Enhanced oil recovery: an update review[J]. Energies, 2010, 3(9): 1529-1575.

[3] Safdel M, Anbaz M A, Daryasafar A, et al. Microbial enhanced oil recovery, a critical review on worldwide implemented field trials in different countries[J]. Renewable and Sustainable Energy Reviews, 2017, 74: 159-172.

[4] Bartels W B, Mahani H, Berg S, et al. Literature review of low salinity waterflooding from a length and time scale perspective[J]. Fuel, 2019, 236: 338-353.

[5] RezaeiDoust A, Puntervold T, Strand S, et al. Smart water as wettability modifier in carbonate and sandstone: A discussion of similarities/differences in the chemical mechanisms[J]. Energy & fuels, 2009, 23(9): 4479-4485.

[6] Katende A, Sagala F. A critical review of low salinity water flooding: mechanism, laboratory and field application[J]. Journal of Molecular Liquids, 2019.

[7] Awolayo A N, Sarma H K, Nghiem L X. Brine-dependent recovery processes in carbonate and sandstone petroleum reservoirs: review of laboratory-field studies, interfacial mechanisms and modeling attempts[J]. Energies, 2018, 11(11): 3020.

[8] Nasralla R A, Bataweel M A, Nasr-El-Din H A. Investigation of wettability alteration and oil-recovery improvement by low-salinity water in sandstone rock[J]. Journal of Canadian Petroleum Technology, 2013, 52(02): 144-154.

[9] Ghanbari E, Dehghanpour H. Impact of rock fabric on water imbibition and salt diffusion in gas shales[J]. International Journal of Coal Geology, 2015, 138: 55-67.

[10] Yousef A A, Al-Saleh S H, Al-Kaabi A, et al. Laboratory investigation of the impact of injection-water salinity and ionic content on oil recovery from carbonate reservoirs[J]. SPE Reservoir Evaluation & Engineering, 2011, 14(05): 578-593.

[11] Al-Anssari S, Barifcani A, Wang S, et al. Wettability alteration of oil-wet carbonate by silica nanofluid[J]. Journal of colloid and interface science, 2016, 461: 435-442.

[12] RezaeiDoust A, Puntervold T, Austad T. Chemical verification of the EOR mechanism by using low saline/smart water in sandstone[J]. Energy & Fuels, 2011, 25(5): 2151-2162.

[13] Shariatpanahi S F, Hopkins P, Aksulu H, et al. Water based EOR by wettability alteration in dolomite[J]. Energy & Fuels, 2016, 30(1): 180-187.

[14] Jackson M D, Al-Mahrouqi D, Vinogradov J. Zeta potential in oil-water-carbonate systems and its impact on oil recovery during controlled salinity water-flooding[J]. Scientific reports, 2016, 6: 37363.

[15] Morrow N R. Wettability and its effect on oil recovery[J]. Journal of petroleum technology, 1990, 42(12): 1,476-1,484.

[16] Sheng J J. Critical review of low-salinity waterflooding[J]. Journal of Petroleum Science and Engineering, 2014, 120: 216-224.

[17] Ershadi M, Alaei M, Rashidi A, et al. Carbonate and sandstone reservoirs wettability improvement without using surfactants for Chemical Enhanced Oil Recovery (C-EOR)[J]. Fuel, 2015, 153: 408-415.

[18] Austad T, RezaeiDoust A, Puntervold T. Chemical mechanism of low salinity water flooding in sandstone reservoirs[C]//SPE improved oil recovery symposium. Society of Petroleum Engineers, 2010.

[19] Fang W Z, Tang Y Q, Ban C, et al. Atomic layer deposition in porous electrodes: A pore-scale modeling study[J]. Chemical Engineering Journal, 2019, 378: 122099.

[20] Jerauld G R, Webb K J, Lin C Y, et al. Modeling low-salinity waterflooding[C]//SPE Annual Technical Conference and Exhibition. Society of Petroleum Engineers, 2006.

[21] Fang C, Sun S, Qiao R. Structure, Thermodynamics, and Dynamics of Thin Brine Films in Oil–Brine–Rock Systems[J]. Langmuir, 2019, 35(32): 10341-10353.

[22] Zhang L, Lu X, Liu X, et al. Distribution and mobility of crude oil-brine in clay mesopores: Insights from molecular dynamics simulations[J]. Langmuir, 2019.

[23] Koleini M M, Badizad M H, Kargozarfard Z, et al. Interactions between rock/brine and oil/brine interfaces within thin brine film wetting carbonates: a molecular dynamics simulation study[J]. Energy & Fuels, 2019.

[24] Fang C, Yang Y, Sun S, et al. Low salinity effect on the recovery of oil trapped by nanopores: A molecular dynamics study[J]. Fuel, 2020, 261: 116443.

[25] Fang C. Pore-scale Interfacial and Transport Phenomena in Hydrocarbon Reservoirs[D]. Virginia Tech, 2019.

[26] Tian H, Wang M. Molecular dynamics for ion-tuned wettability in oil/brine/rock systems[J]. Aip Advances, 2017, 7(12): 125017.

[27] Xu S, Wang J, Wu J, et al. Oil Contact Angles in a Water-Decane-Silicon Dioxide System: Effects of Surface Charge[J]. Nanoscale research letters, 2018, 13(1): 108.

[28] Jiménez-Ángeles F, Firoozabadi A. Contact Angle, Liquid Film, and Liquid–Liquid and Liquid–Solid Interfaces in Model Oil–Brine–Substrate Systems[J]. The Journal of Physical Chemistry C, 2016, 120(22): 11910-11917.

[29] Zhao J, Yao G, Ramisetti S B, et al. Molecular dynamics investigation of substrate wettability alteration and oil transport in a calcite nanopore[J]. Fuel, 2019, 239: 1149-1161.

[30] Do Hong S, Ha M Y, Balachandar S. Static and dynamic contact angles of water droplet on a solid surface using molecular dynamics simulation[J]. Journal of colloid and interface science, 2009, 339(1): 187-195.

[31] Lee K H, Kwon T W, Ha M Y. A Study of Characteristics of Water Droplets on Various Nanoscale Structures Using Molecular Dynamics[J]. Korean Journal of Air-Conditioning and Refrigeration Engineering, 2018, 30(1): 33-43.

[32] Wu J, Ervik Å, Snustad I, et al. Contact Angle and Condensation of a CO2 Droplet on a Solid Surface[J]. The Journal of Physical Chemistry C, 2018, 123(1): 443-451.

[33] Derksen J J. Droplets sliding over shearing surfaces studied by molecular dynamics[J]. AIChE Journal, 2015, 61(11): 4020-4027.

[34] Derksen J J, Komrakova A E. Multiscale simulations of sliding droplets[J]. Acta Mechanica, 2019, 230(2): 657-666.

[35] Martínez L, Andrade R, Birgin E G, et al. PACKMOL: a package for building initial configurations for molecular dynamics simulations[J]. Journal of computational chemistry, 2009, 30(13): 2157-2164.

[36] Momma K, Izumi F. VESTA 3 for three-dimensional visualization of crystal, volumetric and morphology data[J]. Journal of applied crystallography, 2011, 44(6): 1272-1276.

[37] Momma K, Izumi F. VESTA: a three-dimensional visualization system for electronic and structural analysis[J]. Journal of Applied Crystallography, 2008, 41(3): 653-658.

[38] Raiteri P, Gale J D, Quigley D, et al. Derivation of an accurate force-field for simulating the growth of calcium carbonate from aqueous solution: a new model for the calcite− water interface[J]. The Journal of Physical Chemistry C, 2010, 114(13): 5997-6010.

[39] Ballal D, Venkataraman P, Fouad W A, et al. Isolating the non-polar contributions to the intermolecular potential for water-alkane interactions[J]. The Journal of chemical physics, 2014, 141(6): 064905.

[40] Jorgensen W L, Tirado-Rives J. The OPLS [optimized potentials for liquid simulations] potential functions for proteins, energy minimizations for crystals of cyclic peptides and crambin[J]. Journal of the American Chemical Society, 1988, 110(6): 1657-1666.

[41] Fenter P, Kerisit S, Raiteri P, et al. Is the calcite–water interface understood? Direct comparisons of molecular dynamics simulations with specular X-ray reflectivity data[J]. The Journal of Physical Chemistry C, 2013, 117(10): 5028-5042.

[42] Smith W, Yong C W, Rodger P M. DL_POLY: Application to molecular simulation[J]. Molecular Simulation, 2002, 28(5): 385-471.

[43] Santiso E, Herdes C, Müller E. On the calculation of solid-fluid contact angles from molecular dynamics[J]. Entropy, 2013, 15(9): 3734-3745.

[44] Gupta R, Mohanty K K. Wettability alteration mechanism for oil recovery from fractured carbonate rocks[J]. Transport in porous media, 2011, 87(2): 635-652.

[45] Metin C O, Baran J R, Nguyen Q P. Adsorption of surface functionalized silica nanoparticles onto mineral surfaces and decane/water interface[J]. Journal of Nanoparticle Research, 2012, 14(11): 1246.

[46] Alotaibi M B, Azmy R, Nasr-El-Din H A. Wettability challenges in carbonate reservoirs[C]//SPE Improved Oil Recovery Symposium. Society of Petroleum Engineers, 2010.

[47] Soper A K. The radial distribution functions of water and ice from 220 to 673 K and at pressures up to 400 MPa[J]. Chemical Physics, 2000, 258(2-3): 121-137.

[48] Ryckaert J P, Bellemans A. Molecular dynamics of liquid alkanes[J]. Faraday Discussions of the Chemical Society, 1978, 66: 95-106.

[49] Cooke DJ, Gray RJ, Sand KK, Stipp SL, Elliott JA. Interaction of ethanol and water with the {1014} surface of calcite. Langmuir 2010;26(18):14520-14529.

[50] Schellenberger F, Encinas N, Vollmer D, et al. How water advances on superhydrophobic surfaces[J]. Physical review letters, 2016, 116(9): 096101.

[51] Schellenberger F, Xie J, Encinas N, et al. Direct observation of drops on slippery lubricant-infused surfaces[J]. Soft Matter, 2015, 11(38): 7617-7626.

[52] Schellenberger F, Papadopoulos P, Kappl M, et al. Detaching microparticles from a liquid surface[J]. Physical review letters, 2018, 121(4): 048002.